Measurement and statistical analysis of the wavefront distortions induced by atmospheric turbulence using two-channel moiré deflectometry

Measurement and statistical analysis of the wavefront distortions induced by atmospheric turbulence using two-channel moiré deflectometry

Mohsen Dashti[1] **and Saifollah Rasouli**[1,2]

[1] Department of Physics, Institute for Advanced Studies in Basic Sciences (IASBS), Gava Zang,
PO Box 45195-1159, Zanjan 45137-66731, Iran
[2] Optics Research Center, Institute for Advanced Studies in Basic Sciences (IASBS), Gava Zang,
PO Box 45195-1159, Zanjan 45137-66731, Iran

E-mail: rasouli@iasbs.ac.ir

Abstract

Recently, an adjustable, high-sensitivity, wide dynamic range, two-channel wavefront sensor based on moiré deflectometry was proposed by Rasouli *et al* (2010 *Opt. Express* **18** 23906). In this work we have used this sensor on a telescope for measuring turbulence-induced wavefront distortions. A slightly divergent laser beam passes through turbulent ground level atmosphere and enters the telescope's aperture. The laser beam is collimated behind the telescope's focal point by means of a collimator and the beam enters the wavefront sensor. First, from deviations in the moiré fringes we calculate the two orthogonal components of the angle of arrival at each location across the wavefront. The deviations have been deduced in successive frames which allows evolution of the wavefront shape and Fried's seeing parameter r_0 to be determined. Mainly, statistical analysis of the reconstructed wavefront distortions are presented. The achieved accuracy in the measurements and comparison between the measurements and the theoretical models are presented. Owing to the use of the sensor on a telescope, and using sub-pixel accuracy for the measurement of the moiré fringe displacements, the sensitivity of the measurements is improved by more than one order of magnitude. In this work we have achieved a minimum measurable angle of arrival fluctuations equal to 3.7×10^{-7} rad or 0.07 arc s. Besides, because of the large area of the telescope's aperture, a high spatial resolution is achieved in detecting the spatial perturbations of the atmospheric turbulence.

(Some figures may appear in colour only in the online journal)

1. Introduction

One of the most common applications of wavefront sensors is to measure atmospheric turbulence. The requirements are to sense the wavefront with enough spatial resolution and enough speed for real time compensation of atmo-spheric seeing. The lateral shearing interferometer [1], the Shack–Hartmann wavefront sensor [2, 3], and the curvature sensor [4] are the most commonly used sensors in atmospheric turbulence and adaptive optics. Talbot effect and moiré deflectometry have already been employed for wavefront sensing in different fields and in several different ways [5–11].
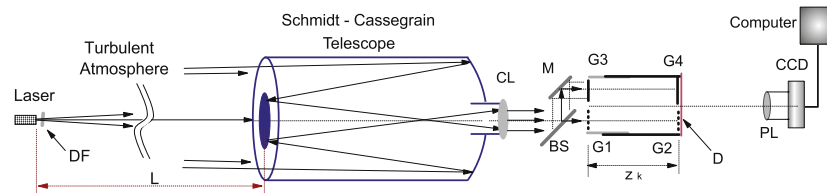
Figure 1. Schematic diagram of the experimental setup. DF, CL, BS, M, D and PL stand for the neutral density filter, collimating lens, beam splitter, mirror, diffuser, and projecting lens, respectively. G1, G2, G3, and G4 stand for the gratings.

However, to the best of our knowledge, moiré deflectometry has not been used for sensing time-varying distortions of wavefronts.

In the last few years, we have introduced some novel methods, based on the moiré technique, for atmospheric turbulence characterization [12–14]. The most significant results of these works are the improvement of the measurement precision and access to a large volume of 2D data—namely, because of the magnifications of the telescope, the use of the moiré technique, and the Talbot effect, measurements of light-beam deflections can be up to two orders of magnitude more precise than other methods such as differential image motion monitor systems [15], generalized seeing monitor systems [16], and the edge image waviness effect [17]. Also, we have used moiré deflectometry for wavefront sensing in various schemes [18, 19]. In this recent scheme, an adjustable, high-sensitivity, wide dynamic range, two-channel wavefront sensor was suggested for measuring distortions of light wavefronts transmitted through the atmosphere [19]. In this sensor, a slightly divergent laser beam is passed through the turbulent ground level atmosphere and then a beam splitter divides it into two beams. The beams pass through a pair of moiré deflectometers which are installed parallel and close together. From deviations in the moiré fringes, two orthogonal components of the angle of arrival (AA) at each location across the wavefront are calculated. The deviations have been deduced in successive frames which allows evolution of the wavefront shape to be determined. The major limitation of this sensor in the study of atmospheric turbulence is the small size of the gratings on the moiré deflectometers that can be used. Practically, constructing large area gratings and employing such gratings in the moiré deflectometers are not straightforward, and feeding the resulting moiré patterns into a CCD needs an elaborate optical system.

Now, in this work we have used this sensor on a telescope for measuring turbulence-induced wavefront distortions. Two components of the AA on the entire area of the telescope's aperture are measured from the data of two channels. Owing to the use of the sensor on the telescope, the sensitivity of the measurements is improved by one order of magnitude. In addition, in this work for the first time we have used sub-pixel resolution for the moiré fringe traces' displacement measurements. This also improves precision of the measurements, remarkably. Besides, because of the large area of the telescope's aperture, a high spatial resolution is achieved in detecting the spatial perturbations of the atmospheric turbulence. Also, in this work statistical analysis

of the reconstructed wavefront distortions are presented. The achieved accuracy in the measurements and comparison between the measurements and the theoretical models are presented.

It should be mentioned that we recently suggested the use of a one-channel moiré deflectometer on a telescope for atmospheric turbulence measurements [14]. However, it was recognized that the device was sensitive to the incoming wavefront changes only in one direction normal to the gratings' rulings. This is the major limitation of the mentioned work for wavefront sensing.

2. Moiré deflectometry

A moiré pattern appears when two similar gratings are superimposed at a small angle or when they have slightly different periods. In many applications of the moiré pattern, one of the superimposed gratings is the image of a physical grating or is one of the self-images of the first grating [20]. By illuminating a grating with a spatially coherent light beam, exact images and many other images of the grating can be created at finite distances from the grating. This self-imaging phenomenon is called the Talbot effect. A moiré deflectometer consists of two gratings, in which the second grating is installed at the plane of one of the self-images of the first grating and the inspected object is placed in front the first grating. The moiré deflectometry measures ray deflections in the paraxial approximation induced by the phase object. The resulting moiré fringe pattern is a map of ray deflections corresponding to the optical properties of the inspected object. Generally, when the image forming light propagates in a perturbed medium the self-image is distorted and the distortion is magnified by the moiré pattern.

3. Experimental setup

A schematic diagram of the experimental setup is shown in figure 1. A slightly divergent laser beam passes through turbulent ground level atmosphere and enters the telescope's aperture. The laser beam is collimated behind the telescope's focal point by means of a collimator. The collimated beam passes through a beam splitter, and the resulting beams pass through a pair of moiré deflectometers which are installed parallel and close together [19]. The moiré deflectometers are installed quite close to each other. The directions of the gratings' rulings are almost parallel in each moiré deflectometer but are perpendicular in the two beams. Moiré

patterns are formed on a plane where the second gratings of the moiré deflectometers and a diffuser are installed. The moiré patterns from both beams are projected on a CCD camera. Successive moiré patterns are recorded by the CCD camera and transferred to a computer, to allow temporal fluctuations of the wavefront phase to be measured highly accurately. Displacements of the moiré fringes in the recorded patterns correspond to the fluctuations of two orthogonal components of the AA across the wavefront. The fluctuations are deduced in successive frames, and the evolution of the wavefront shape is determined.

In the presented measurements, since the power of the laser source was sufficient, the exposure time of the frames was a small part of the sampling period. The exposure time of the frames and the sampling period were 1/900 s and 60 frames s^{-1}, respectively. This guarantees the evolution of the wavefronts between successive frames without any time-averaging on the wavefronts. Besides, by using a high-speed CCD, the frame sampling rate can be selected faster than the atmospheric distortion changes, and as a result unrealistic discontinuities in the wavefronts from frame to frame do not occur. For low light applications as one would normally expect in astronomy (to work with stars), the sensor can be set up using phase gratings on a large-sized telescope. Using a high-sensitivity CCD camera will also help in low light applications. It seems that using a laser guide star one can also overcome this limitation.

4. Theoretical framework

In the theoretical considerations we assume that a wavefront enters the telescope's aperture of diameter D with a local AA on that plane, α. On the image plane of the pupil, we have a wavefront of diameter $D' = \gamma D$, and the corresponding AA is equal to [14]

$$\alpha' = \frac{\alpha}{\gamma}, \qquad (1)$$

where γ is the magnification of the optical system given by $\gamma = \frac{f'}{f}$, f is the telescope's focal length, and f' is the focal length of the collimating lens. The collimated beam enters the wavefront sensor. In the sensor, we have used two moiré deflectometers in two channels. We choose a coordinate system so that in the first channel the grating rulings are in the x-direction and those in the second channel are in the y-direction, as shown in figure 1. The laser beam splits into two beams by an amplitude beam splitter. The second beam is reflected by a mirror, M, in a direction parallel to the first beam's propagation direction. The beams strike the first gratings G1 and G3, respectively. The second gratings of the moiré deflectometers, G2 and G4 are separated by z_k along its corresponding optical axis, where z_k is the kth Talbot distance of the first gratings. The formula for the kth Talbot distance is $z_k = 2kd^2/\lambda$, where d and λ are the grating's period and the wavelength, respectively. All gratings have equal periods d. Due to the atmospheric turbulence the self-images of the first gratings fluctuate on the second gratings. The components α'_y and α'_x of the AA fluctuation in a direction perpendicular to

the lines of the gratings (parallel to the moiré trace) on the first gratings G1 and G2 are given by [19]

$$[\alpha'_x, \alpha'_y] = \frac{d}{z_k} \left[\frac{\Delta y_{\rm m}}{d'_{\rm m}}, \frac{\Delta x_{\rm m}}{d_{\rm m}} \right], \qquad (2)$$

respectively, where $d_{\rm m}$ and $d'_{\rm m}$ are the moiré fringe spacings, and $\Delta x_{\rm m}$ and $\Delta y_{\rm m}$ are the moiré fringe shifts in the first and second channels, respectively.

Using $\alpha = \gamma \alpha'$ in equation (2) we obtain

$$[\alpha_x, \alpha_y] = \frac{f'}{f} \frac{d}{z_k} \left[\frac{\Delta y_{\rm m}}{d'_{\rm m}}, \frac{\Delta x_{\rm m}}{d_{\rm m}} \right]. \qquad (3)$$

According to equation (3), by increasing the gratings' distance or decreasing the period of the gratings, the measurement precision can be improved. Compared to equation (4) of [19], here due to use of the telescope an improving factor $\frac{f'}{f}$ appears. That means for a given resolution of a detecting system such as a CCD camera, by using the telescope, smaller values of AA fluctuations can be measured.

Now, let us estimate the accuracy of the measurements. Using a fitting algorithm on the intensity profile of the moiré fringes, sub-pixel resolution can be achieved in the displacement measurement of a trace [21, 22]. We stipulate the minimum measurable displacement of a trace in the CCD's plane is determined to within sub-pixel accuracy that is $(\Delta y_{\rm m})_{\rm min} = (\Delta x_{\rm m})_{\rm min} = \frac{1 \text{ pixel}}{N}$, where N is an integer. Also, if $d'_{\rm m}$ and $d_{\rm m}$ are covered by M pixels, the minimum measurable AA change is determined by

$$(\alpha_x)_{\rm min} = (\alpha_y)_{\rm min} = \frac{1}{MN} \frac{f'}{f} \frac{d}{z_k}. \qquad (4)$$

Here, an improving factor $\frac{f'}{f}$ appears, due to the use of the telescope. Another improving factor $\frac{1}{N}$ appears, due to the use of the sub-pixel accuracy for the trace displacement measurements. Also, the minimum measurable values of $(\alpha_x)_{\rm min}$ and $(\alpha_y)_{\rm min}$ are influenced by the number of CCD pixels which are covered by the moiré fringes spacing. By using a high-resolution CCD, $d_{\rm m}$ would be covered by a larger number of pixels and, as a result, the accuracy of the measurements can be improved. It should be mentioned that for a low power light beam, for example when it comes from a celestial object, by spreading it over more pixels the signal-to-noise ratio is decreased. But, in our case because the power of the laser is sufficient even for the mentioned case, it is still possible to improve the accuracy of the measurements without paying a toll in the signal-to-noise ratio. In brief, by increasing the gratings' distance, increasing the M and N numbers, or decreasing the period of the gratings and decreasing the factor $\frac{f'}{f}$, the measurement precision can be improved.

In this work, we have used $d = \frac{1}{15}$ mm, $f = 200$ cm, $f' = 20$ cm, and $z_k = 69$ mm. The value of z_k of 69 mm corresponds to $k = 5$. The moiré pattern in each channel consists of about 238 pixels × 238 pixels and $d_{\rm m}$ was covered by 26 pixels ($M = 26$ pixels) in both channels. By considering $N = 10$ [23], the minimum measurable AA fluctuation is 3.7×10^{-7} rad or 0.07 arc s. It should be mentioned that

compared to [19], in this work we have used $z_k = 69$ mm instead of $z_k = 224$ mm.

On the other hand, if we stipulate that the maximum measurable displacement of a trace is equal to half the moiré fringe spacing, $(\frac{\Delta y_m}{d'_m})_{max} = (\frac{\Delta x_m}{d_m})_{max} = \frac{1}{2}$, according to equation (3), AA fluctuations in the range $-\frac{1}{2}\frac{f'}{f}\frac{d}{z_k}$ to $+\frac{1}{2}\frac{f'}{f}\frac{d}{z_k}$ would be measured. Thus, for the above-mentioned values of the experimental parameters, one can measure AA fluctuations in the range -17 to $+17$ arc s without making any adjustment in the setup.

Since α_x and α_y are equal to the incident wavefront gradients in x- and y-directions, respectively, the incident wavefront gradients at a given point are determined by

$$\left[\frac{\partial U}{\partial x}, \frac{\partial U}{\partial y}\right] = \frac{f'}{f}\frac{d}{z_k}\left[\frac{\Delta y_m}{d'_m}, \frac{\Delta x_m}{d_m}\right]. \tag{5}$$

5. Experimental work

In the experiment a He–Ne laser beam passes through a turbulent surface layer of the atmosphere and enters the telescope (the Meade 8 inch Schmidt–Cassegrain model) aperture. The source and the experimental setup are installed at a height of 85 cm, over an asphalted area, at a distance of 360 m from each other. The collimating lens CL of focal length 20 cm is used for collimation of the beam. In the experiment G2 and G4 are installed at a distance of 69 mm from G1 and G3 respectively. All the gratings are identical and have a ruling period of 1/15 mm. Moiré patterns are formed on a plane where the G2 and G4 and a diffuser, D, are installed. Using a projection lens, PL, both of the moiré patterns are projected on a CCD (The Imaging Source, model DMK 21AU04, USB CCD Monochrome Camera) which is connected to a computer. After alignment of the setup, the beam intensity was reduced by a neutral density filter to a level below the saturation level of the CCD. The moiré fringes were recorded by a sampling rate 60 frames s^{-1}.

Several sets of experimental data were recorded and digitized. In this report, we refer to the typical series of the measurements performed on 12 May 2012. Each set of data was collected in 33 s and contained 2000 frames. A typical recorded frame is shown in figure 2(a). To get clearer fringes, the high-frequency illumination of the pattern i.e. the image of the grating lines, is removed by fast Fourier transform using MATLAB software, figure 2(b). The background movie of figure 2, contains 300 successive recorded patterns (video-2 available at stacks.iop.org/JOpt/14/095704/mmedia). The traces of bright and dark moiré fringes and the first-order virtual traces were derived. We call the traces of points with intensities equal to the mean intensity of the adjacent bright and dark traces, the first-order virtual traces [19]. In this work, we have determined the traces within pixel/10 accuracy. A single moiré dark fringe, the intensity distribution on its neighborhood after the fast Fourier transforming process, and the corresponding derived trace within one pixel accuracy and within pixel/10 accuracy are shown in figures 3(a)–(c) and (e), respectively. In figures 3(d)
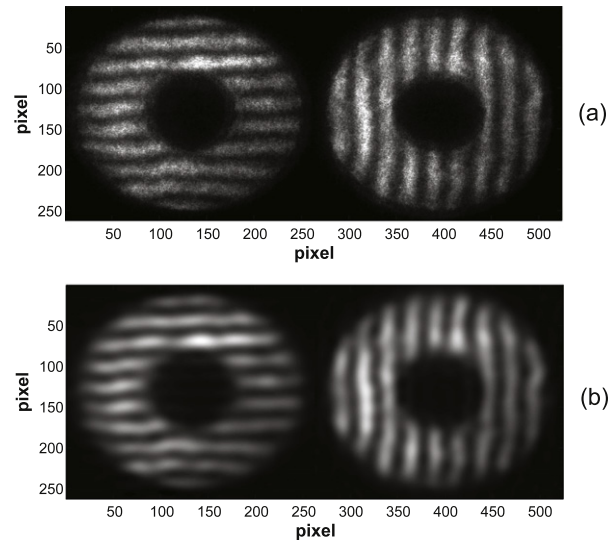

Figure 2. (a) A typical recorded frame consists of two sets of orthogonal moiré patterns and (b) the corresponding low-frequency illumination distribution, (Video-2 available at stacks.iop.org/JOpt/14/095704/mmedia). The moiré pattern in each channel consists of about 238 pixels × 238 pixels. One pixel resolution in the image is equal to 0.85 mm in the real space on the telescope's aperture plane.

and (f) a small part of the derived trace of the dark fringe using one pixel and within pixel/10 accuracy is shown. Figure 3(f) shows how well a trace of a given moiré fringe can be determined as a fraction of a pixel. For all the bright, dark, and the first-order virtual traces of the moiré fringes, the intersection points are determined.

In these experiments, 756 intersection points out of an array of 35 × 33 points were used for wavefront reconstruction. The distance between two adjacent intersection points corresponds to 5.2 mm in real space on the telescope's aperture plane. It should be mentioned that compared to the Shack–Hartmann wavefront sensor, the maximum number of correctable terms for modal compensation can be about 1/5 of the intersection points [24]. The displacement vectors of the intersection points were calculated with respect to their mean positions. From the magnitude of the displacements in the x and y directions and using equation (5) the wavefront gradients in the corresponding directions were obtained. A plot of the reconstructed wavefront surface, corresponding to distortions generated by the atmospheric turbulence is shown in figure 4(a). The data sets were recorded at 23:10 pm (12 May 2012).

In parallel with the above-mentioned measurements, we have measured Fried's seeing parameter r_0 using the differential image motion monitor (DIMM) [15] and the method was proposed in [14]. For the DIMM measurements we used the setup shown in figure 1 with some changes. We replaced the laser source with a point source and used a mask consisting of two widely separated small apertures in front of the telescope's aperture. We removed the sensor and used a CCD near the back focal plane of the telescope. Other parameters were the same as those mentioned for the setup in figure 1. In the DIMM experiment, the apertures were 12 cm apart and had a diameter of 4 cm. A CCD (DCC1545M—high
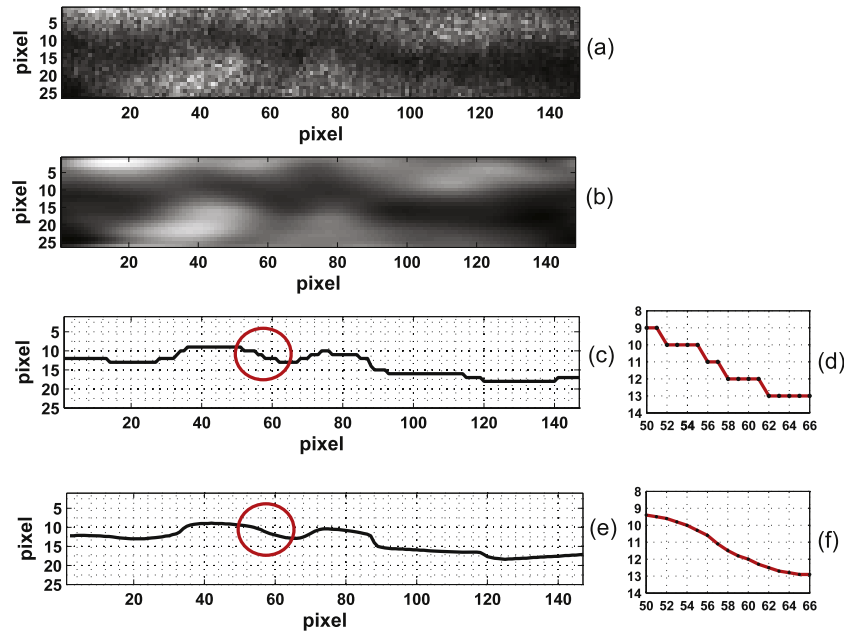
Figure 3. (a) Sample moiré dark fringe, (b) low-frequency illumination distribution on the area containing the dark fringe, (c) derived trace of the dark fringe within one pixel accuracy, (e) derived trace of the dark fringe within pixel/10 accuracy. In (d) and (f) a small part of the derived trace of the dark fringe using one pixel accuracy and within pixel/10 accuracy, respectively, is shown. The locations of the selected parts are shown in (c) and (e) by red circles.
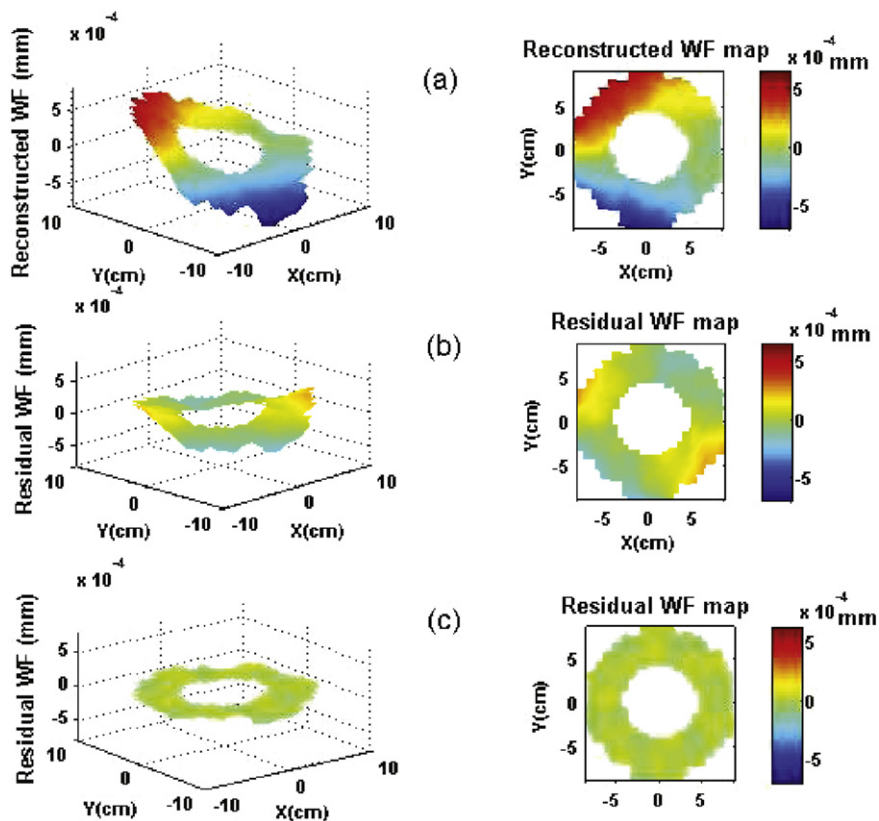

Figure 4. (a) Reconstructed wavefront map, (b) the corresponding tip and tilt removed residual wavefront map, and (c) the corresponding residual wavefront map after removing the first 20 aberrations (Video-4 available at stacks.iop.org/JOpt/14/095704/mmedia).

resolution USB2.0 CMOS Camera, Monochrome) was used for recording successive frames. The sampling rate was 60 frames s^{-1} and the exposure time for a frame was 12 ms. The data sets of the DIMM method were recorded at 23:15 pm

(12 May 2012). A typical recorded frame using the DIMM method is shown in figure 5. The background movie of figure 5, contains 300 successive recorded frames (video-5 available at stacks.iop.org/JOpt/14/095704/mmedia). The *x*
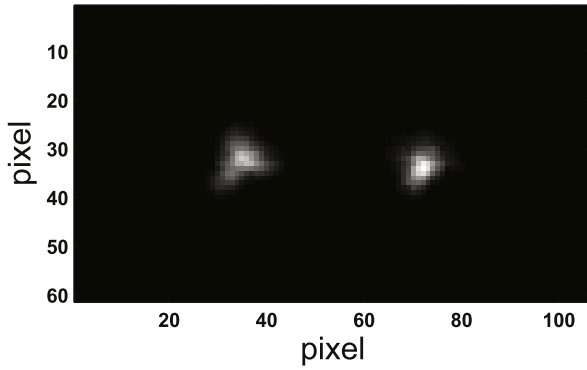
Figure 5. A typical recorded frame of the DIMM method, the background movie contains 300 successive frames (video-5 available at stacks.iop.org/JOpt/14/095704/mmedia).

Table 1. Zernike–Kolmogorov residual errors (σ_J^2) [25] and the corresponding calculated Fried's seeing parameter r_0. (D is the diameter of the telescope's aperture.)

σ_J^2	r_0 (cm)
$\sigma_3^2 = 0.134 \left(\frac{D}{r_0}\right)^{5/3}$	4.89 ± 0.08
$\sigma_6^2 = 0.0648 \left(\frac{D}{r_0}\right)^{5/3}$	4.96 ± 0.14
$\sigma_9^2 = 0.0463 \left(\frac{D}{r_0}\right)^{5/3}$	5.17 ± 0.24
$\sigma_{14}^2 = 0.0304 \left(\frac{D}{r_0}\right)^{5/3}$	5.31 ± 0.42
$\sigma_{17}^2 = 0.0255 \left(\frac{D}{r_0}\right)^{5/3}$	5.40 ± 0.53
$\sigma_{20}^2 = 0.0220 \left(\frac{D}{r_0}\right)^{5/3}$	5.67 ± 0.72

and y components of the AA fluctuations were measured from the displacements of the image points. The time series of the x and y components of the AA fluctuations at the apertures are shown in figure 6. In this method, using the variance of the differential longitudinal motion of the image points [15]

$$\sigma_l^2 = 2\lambda^2 r_0^{-5/3}[0.179D^{-1/3} - 0.096\text{d}^{-1/3}],$$

the value of r_0 can be determined. Here, λ, d, and D are the wavelength, the apertures' distance, and the diameter of the apertures, respectively. For the experimental values $D = 40$ mm, $\delta D = 1$ mm, $d = 120$ mm, $\delta d = 1$ mm, $\sigma_l^2 = 2.36 \times 10^{-11}$ rad^2, and $\delta(\sigma_l^2) = 6.77 \times 10^{-12}$ rad^2, the value of r_0 and its absolute error are obtained as 5.6 cm and 0.96 cm, respectively. For more details of the DIMM method see [15].

6. Statistical analysis of the reconstructed wavefront distortions

Now, let us go back to our method and consider the wavefront over the telescope's aperture of diameter D. If a plane wave is fitted to the reconstructed wavefront over the aperture's area, and its phase is subtracted from the wavefront phase (wavefront tip and tilt removal), then the mean square phase distortion over the area is related to Fried's seeing parameter r_0 by [25, 26]

$$\sigma_3^2 = 0.134 \left(\frac{D}{r_0}\right)^{5/3}, \tag{6}$$

where σ_3^2 has the form

$$\sigma_3^2 = \left\langle \frac{4\pi^2}{\lambda^2 \Sigma} \int_\Sigma |U_{\text{res}}(\mathbf{x})|^2 \, d^2\mathbf{x} \right\rangle. \tag{7}$$

Here, the integral is calculated over the area of the reconstructed wavefront, Σ, the brackets $\langle \rangle$ represent an ensemble average, λ is the wavelength, and U_{res} is the residual wavefront after piston, tip, and tilt removal. For the reconstructed wavefront of figure 4(a), the residual wavefront surface plot after the removal of the piston tip and tilt is shown in figure 4(b). The mean square phase distortion of

the residual wavefronts for the data sets of 2000 successive frames is calculated. Using equation (6), the value of $r_0 = 4.89 \pm 0.08$ cm is obtained. As mentioned earlier, we have measured r_0 by using the differential image motion monitor (DIMM) [15] and the method was proposed in [14]. The results are compatible.

Now, let us examine the above-mentioned procedure on the reconstructed wavefront when the first J modes are corrected. The σ_J^2 value for $J = 3, 6, 9, 14, 17, 20$ and the corresponding, calculated, Fried's seeing parameter r_0 are shown in table 1. Theoretical considerations of the modal wavefront representation in terms of the Zernike modes can be found in the paper by [25]. As previously mentioned, compared to the Shack–Hartmann wavefront sensor, the maximum number of correctable terms for modal compensation can be about 1/5 of the intersection points [24]. We have used 756 intersection points for wavefront reconstruction. The residual wavefront surface plot, after removing the first 20 aberrations, corresponding to the reconstructed wavefront of figure 4(a), is shown in figure 4(c). The background movie of figure 4 shows the evolution of the wavefront and the corresponding residual wavefronts in 300 successive frames (video-4 available at stacks.iop.org/JOpt/14/095704/mmedia).

In figure 7, the sum of the lowest order aberrations of the reconstructed wavefront map is shown. The background movie of figure 7 shows the evolution of the additional lowest order aberrations in 300 successive frames (video-7 available at stacks.iop.org/JOpt/14/095704/mmedia).

In figure 8, we have plotted the experimental and the Kolmogorov theoretical prediction of variance of the compensated wavefront which are a fraction of the variance of the uncompensated wavefront, i.e. the ratio σ_J^2/σ_1^2 against a function of the number J. The experimental plot is compatible with the results predicted by the theoretical calculation [26]. Meanwhile, it is worth mentioning that the residual wavefront errors show a systematic trend that is a little lower than the Kolmogorov prediction.

This device can be used to characterize spatially and temporally the statistics of the wavefront phase. In this regard, the phase structure function of the light beam propagating through atmospheric turbulence can be used to characterize
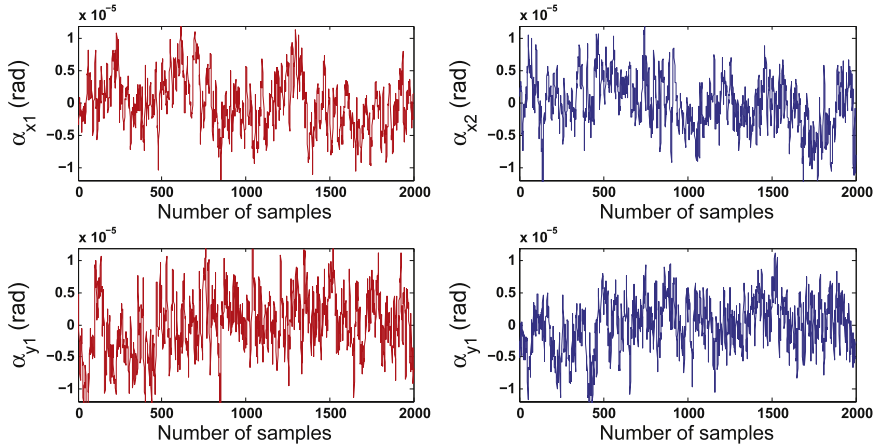
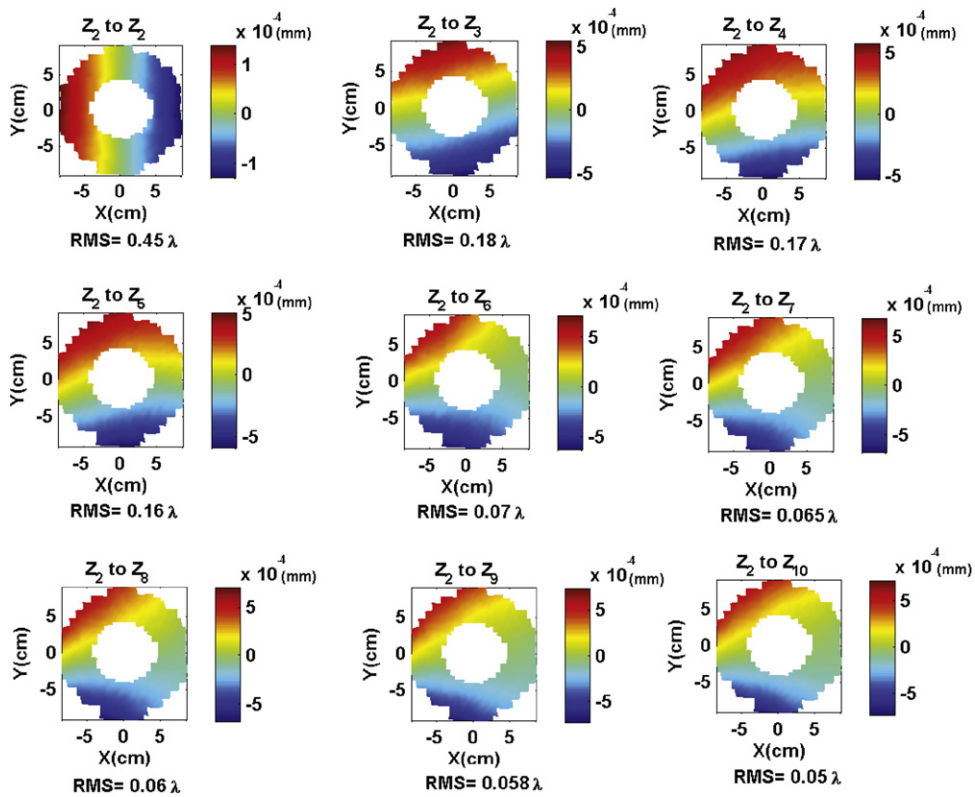**Figure 6.** *x* and *y* components of AA fluctuations at the apertures in the DIMM method versus time.

Figure 7. Map of the sum of the lowest order aberrations of the reconstructed wavefront (video-7 available at stacks.iop.org/JOpt/14/095704/mmedia).

the spatial properties of the wavefront. In the next section, using the phase structure function of the reconstructed wavefront, Fried's seeing parameter r_0 will be estimated.

7. Phase structure function

The phase variance between two separate points on the wavefront is defined as the phase structure function and is given by [26]

$$D_\phi(\xi) = \langle |\phi(r) - \phi(r + \xi)|^2 \rangle, \qquad (8)$$

where ϕ is the wavefront phase, ξ is the separation distance between two points on the wavefront, and $\langle \cdots \rangle$ represents an ensemble average. We have measured the phase structure function, $D_\phi(\xi)$, by measuring the difference of phase between pairs of points, with a given value of separation ξ, displaced spatially on the reconstructed wavefront on the telescope aperture. We have done these calculations for all of the successive reconstructed wavefronts. The variance of the difference is the structure function of the phase for the given value of ξ. Now, by repeating the process for other possible values of ξ, the phase structure function, $D_\phi(\xi)$, can be determined as a function of ξ. Fried has shown that
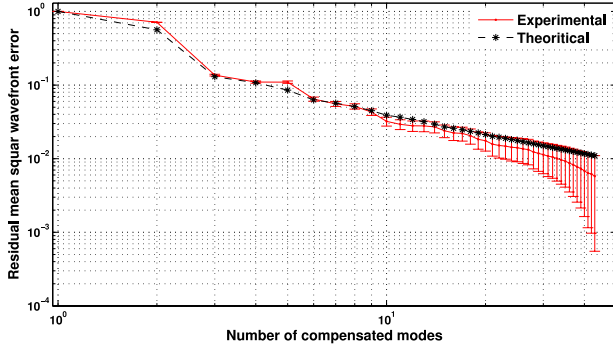
Figure 8. Experimental and the Kolmogorov theoretical prediction of residual mean square wavefront distortion σ_J^2/σ_1^2 as a function of the number J of compensated modes.
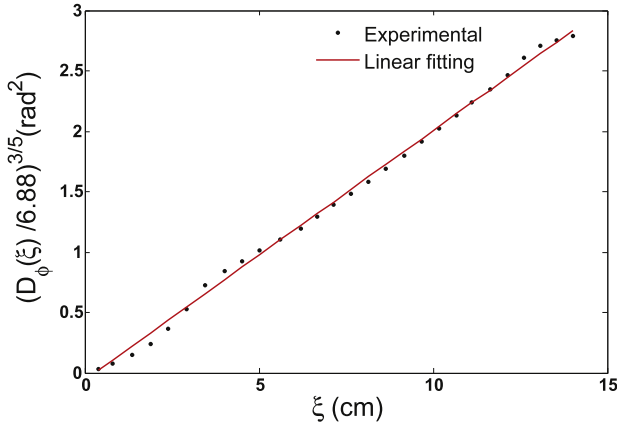

Figure 9. Fried's seeing parameter is obtained from the phase structure function of the reconstructed wavefront.

the phase structure function in the Kolmogorov model of atmospheric turbulence is given by [26]

$$D_\phi(\xi) = 6.88 \left(\frac{\xi}{r_0} \right)^{5/3}, \tag{9}$$

where again r_0 is Fried's seeing parameter. Then, by plotting $D_\phi^{3/5}$ with respect to ξ and using a simple fitting method one can evaluate the value of r_0. In figure 9, the experimental data and the fitting curve are shown. The measured value of the slope of the fitted line is 0.209 ± 0.002 cm^{-1} and it is equal to the inverse of Fried's seeing parameter; $r_0 = 4.9 \pm 0.04$ cm. This value of r_0 is compatible with the result obtained from the statistical analysis of the reconstructed wavefront distortions.

8. Error analysis of the measurements

8.1. Wavefront gradient error estimation

Using equations (1) and (3), the wavefront gradient or the AA on the telescope's aperture is related to the moiré fringe displacements Δy_m by

$$\alpha_x = \frac{\gamma d}{d_m z_k} \Delta y_m. \tag{10}$$

The uncertainty or error in the AA measurement can be found by using the rules of propagation of uncertainties. If the original uncertainties are independent and random, the uncertainties are added in quadrature [27]. Therefore, the error of the wavefront slope measurement is calculated from

$$\frac{\delta\alpha_x}{\alpha_x} = \\ \sqrt{\left(\frac{\delta\gamma}{\gamma}\right)^2 + \left(\frac{\delta d}{d}\right)^2 + \left(\frac{\delta(\Delta y_m)}{\Delta y_m}\right)^2 + \left(\frac{\delta d_m}{d_m}\right)^2 + \left(\frac{\delta z_k}{z_k}\right)^2}, \tag{11}$$

where δ shows the measurement error of the corresponding parameter; for example, δd_m and δz_k are the reading errors of the moiré fringe period and the Talbot distance, respectively. In order to achieve high precision, all quantities and their errors should be measured with a high resolution. For typical experimental values $\gamma = 0.1$, $d = \frac{1}{15}$ mm, $d_m = 26$ pixels, $\Delta y_m = 8$ pixels, $z_k = 69$ mm, $\delta\gamma =$ negligible, $\delta d =$ negligible, $\delta d_m = \frac{1}{10}$ pixel, $\delta(\Delta y_m) = \frac{1}{10}$ pixel, and $\delta z_k = 1$ mm, the AA value and its absolute error are obtained as 2.9×10^{-5} rad and 5.6×10^{-7} rad, respectively. In comparison with the analysis presented in section 4, here the roles of all of the measured quantities have been considered.

8.2. Wavefront error estimation

The wavefront slope at a grid point (or intersection point) is given by [28, 29]

$$\alpha_{x_{ij}} = \frac{U_{ij} - U_{ij+1}}{\ell}, \tag{12}$$

where i and j are the indices of the grid points, ℓ is the distance between two adjacent grid points, and U shows the wavefront shape. Now we can write

$$\alpha_{x_{ij}}\delta\ell + \ell\delta\alpha_{x_{ij}} = \delta U_{ij} - \delta U_{ij+1}.$$

By considering $\delta U_{ij} \simeq \delta U_{ij+1} = \delta U$ we obtain

$$\delta U = \frac{\alpha_{x_{ij}}\delta\ell + \ell\delta\alpha_{x_{ij}}}{2}. \tag{13}$$

For the experimental values $\ell = 5.2$ mm, $\delta\ell = 0.08$ mm, $\alpha_x = 2.9 \times 10^{-5}$ rad, and $\delta\alpha_x = 5.6 \times 10^{-7}$ rad, the absolute error in the wavefront estimation at a given grid point is $\delta U = 2.6 \times 10^{-6}$ mm or $\delta U = \frac{\lambda}{240}$, where λ is the wavelength and its value is 633 nm. By considering $\phi = \frac{2\pi}{\lambda} U$, the absolute error of the measured wavefront phase is $\delta\phi = 0.026$ rad.

8.3. Error estimation of the Zernike coefficients

Zernike polynomials expansion of the phase function is given by [25]

$$\phi = \sum_{i=1}^{\infty} a_i Z_i. \tag{14}$$

We can treat the above equation as a vector matrix multiplication by [30]

$$\mathbf{\Phi} = \mathbf{ZA}, \tag{15}$$

where $\mathbf{Z}$ is a matrix in which each column is one of the annular Zernike polynomials, $\mathbf{A}$ is a column vector of Zernike coefficients, and $\mathbf{\Phi}$ is a column vector of phase values at the grid points. Now, we can find $\mathbf{A}$ from

$$\mathbf{A} = (\mathbf{Z}^{\mathrm{T}}\mathbf{Z})^{-1}\mathbf{Z}^{\mathrm{T}}\mathbf{\Phi}. \qquad (16)$$

Errors in the phase values cause errors in the Zernike coefficients determined by

$$\delta\mathbf{A} = (\mathbf{Z}^{\mathrm{T}}\mathbf{Z})^{-1}\mathbf{Z}^{\mathrm{T}}\delta\mathbf{\Phi}. \qquad (17)$$

We denote $\delta\mathbf{\Phi}$ as a column vector of phase errors at the grid points, $\delta\mathbf{A}$ as a column vector of Zernike coefficient errors, and T as the transposition operator. In this work by considering errors of the measurements, as an example, we obtained the absolute error $\delta a_3 = 0.004$ rad for the Zernike coefficient $a_3 = -1.197$ rad.

8.4. Phase variance error estimation

The mean square residual wavefront error is given by [25]

$$\sigma_J^2 = \left\langle \phi^2 \right\rangle - \sum_{i=1}^{J} \left\langle |a_i|^2 \right\rangle, \qquad (18)$$

where J is the number of compensated Zernike modes. If we remove the piston term in the reconstruction algorithm, then we have $\sigma_1^2 = \left\langle \phi^2 \right\rangle$ and we can write equation (18) as

$$\sigma_J^2 = \sigma_1^2 - \sum_{i=2}^{J} \langle |a_i|^2 \rangle. \qquad (19)$$

Also, we have

$$\sigma_2^2 = \sigma_1^2 - \langle |a_2|^2 \rangle$$
$$\vdots$$
$$\sigma_J^2 = \sigma_{J-1}^2 - \langle |a_J|^2 \rangle. \qquad (20)$$

Now, we can write errors of the residual wavefront after removing J 'Zernike modes' by a recursion equation as

$$\delta\sigma_J^2 = \delta\sigma_{J-1}^2 + \langle \delta |a_J|^2 \rangle. \qquad (21)$$

For example, we obtained the absolute error $\delta\sigma_3^2 = 0.025$ rad^2 for $\sigma_3^2 = 1.43$ rad^2. This error analysis was applied to all the measurements reported in this work.

9. Conclusion

Using a moiré deflectometry based, two-channel wavefront sensor on a telescope, wavefront distortions induced by the atmospheric turbulence are measured. Compared to our previously proposed two-channel wavefront sensor [19], owing to the use of the sensor on a telescope, and using sub-pixel accuracy for the measurement of the moiré fringe displacements, the sensitivity of the measurements is improved by more than one order of magnitude. Besides, because of the large area of the telescope's aperture, a high spatial resolution is achieved in detecting the spatial

perturbations of the atmospheric turbulence. Owing to the first advantage, the device can be used for the study of dilute turbulences, such as a quantum turbulence, in the laboratory. Also, because of the large area of the telescope's aperture, this instrument is more suitable for studying the spatial and temporal properties of wavefronts. A potential application of the instrument in this regard is measuring anisotropy in atmospheric turbulence, which was done recently by the use of one-channel moiré deflectometry on a telescope [31]. The technique is very flexible and can be applied in a wide range of turbulence strengths by choosing gratings of adequate pitch, size, and separation. Since we measure the displacements of the traces in the recorded patterns with respect to their reference positions, the measurement is relatively insensitive to the alignment of the beam with the sensor. In other words, the misalignment of the beam and the optical axis of the sensor causes displaced and deformed traces that do not affect the measurements to any significant extent. The instrument can be used with a white light source such as a celestial object or a laser guide star and it can be used in adaptive optics in astronomy. For low light applications, as one would normally expect in astronomy, the sensor can be used with phase gratings on a large-sized telescope.

Acknowledgments

References

[1] Leibbrandt G W R, Harbers G and Kunst P J 1996 Wavefront analysis with high accuracy by use of a doublegrating lateral shearing interferometer *Appl. Opt.* **35** 6151–61

[2] Shack R V and Platt B C 1971 Production and use of a lenticular Hartmann screen *J. Opt. Soc. Am.* **61** 656

[3] Platt B C and Shack R 2001 History and principles of Shack–Hartmann wavefront sensing *J. Refract. Surg.* **17** S573–7

[4] Roddier E 1988 Curvature sensing and compensation: a new concept in adaptive optics *Appl. Opt.* **27** 1223–5

[5] Canabal H, Quiroga J A and Bernabeu E 1998 Improved phase-shifting method for automatic processing of moiré deflectograms *Appl. Opt.* **37** 6227–33

[6] Legarda-Saenz R 2007 Robust wavefront estimation using multiple directional derivatives in moiré deflectometry *Opt. Lasers Eng.* **45** 915–21

[7] Rottenkolber M and Podbielska H 1996 Measuring ophthalmologic surfaces by means of moiré deflectometry *Opt. Eng.* **35** 1124–33

[8] Quiroga J A, Crespo D and Bernabeu E 1999 Fourier transform method for automatic processing of moiré deflectograms *Opt. Eng.* **38** 974–82

[9] Siegel C, Loewenthal F and Balmer L E 2001 A wavefront sensor based on the fractional Talbot effect *Opt. Commun.* **194** 265–75

[10] Sekine R, Shibuya T, Ukai K, Komatsu S, Hattori M, Mihashi T, Nakazawa N and Hirohara Y 2006 Measurement of wavefront aberration of human eye using Talbot image of two-dimensional grating *Opt. Rev.* **13** 207–11

[11] Salama N H, Patrignani D, Pasquale L D and Sicre E E 1999 Wavefront sensor using the Talbot effect *Opt. Laser Technol.* **31** 269–72

[12] Rasouli S and Tavassoly M T 2006 Application of moiré technique to the measurement of the atmospheric turbulence parameters related to the angle of arrival fluctuations *Opt. Lett.* **31** 3276–8

[13] Rasouli S and Tavassoly M T 2008 Application of the moiré deflectometry on divergent laser beam to the measurement of the angle of arrival fluctuations and the refractive index structure constant in the turbulent atmosphere *Opt. Lett.* **33** 980–2

[14] Rasouli S 2010 Use of a moiré deflectometer on a telescope for atmospheric turbulence measurements *Opt. Lett.* **35** 1470–2 and references 3–4 therein

[15] Sarazin M and Roddier F 1990 The ESO differential image motion monitor *Astron. Astrophys.* **227** 294–300

[16] Ziad A, Conan R, Tokovinin A, Martin F and Borgnino J 2000 From the grating scale monitor to the generalized seeing monitor *Appl. Opt.* **39** 5415–25

[17] Belen'kii M S, Stewart J M and Gillespie P 2001 Turbulence-induced edge image waviness: theory and experiment *Appl. Opt.* **40** 1321–8

[18] Rasouli S, Ramaprakash A N, Das H K, Rajarshi C V, Rajabi Y and Dashti M 2009 Two channel wavefront sensor arrangement employing moiré deflectometry *Optics in Atmospheric Propagation and Adaptive Systems XII; Proc. SPIE* **7476** 74760K

[19] Rasouli S, Dashti M and Ramaprakash A N 2010 An adjustable, high sensitivity, wide dynamic range two channel wavefront sensor based on moiré deflectometry *Opt. Express* **18** 23906–15

[20] Rasouli S 2012 Atmospheric turbulence characterization and wavefront sensing by means of the moiré deflectometry

Topics in Adaptive Optics ed R K Tyson, InTech, Available from: www.intechopen.com/articles/show/title/atmospheric-turbulence-characterization-and-wavefront-sensing-by-means-of-the-moir-deflectometry

[21] Feng Y, Goree J and Liu B 2007 Accurate particle position measurement from images *Rev. Sci. Instrum.* **78** 053704

[22] Anthony S M and Granick S 2009 Image analysis with rapid and accurate two-dimensional Gaussian fitting *Langmuir* **25** 8152–60

[23] Zhang Y, Yang D and Cui X 2004 Measuring seeing with a Shack–Hartmann wave-front sensor during an active-optics experiment *Appl. Opt.* **43** 729–34

[24] Takato N, Iye M and Yamaguchi I 1994 Wavefront reconstruction error of Shack–Hartmann wavefront sensors *Publ. Astron. Soc. Pac.* **106** 182–8

[25] Noll R J 1976 Zernike polynomials and atmospheric turbulence *J. Opt. Soc. Am.* **66** 207–11

[26] Roddier F 1999 *Adaptive Optics in Astronomy* (Cambridge: Cambrige University Press)

[27] Taylor J R 1997 *An Introduction to Error Analysis* (Sausalito, CA: University Science Books)

[28] Herrmann J 1980 Least-squares wave front errors of minimum norm *J. Opt. Soc. Am.* **70** 28–35

[29] Hunt B R 1979 Matrix formulation of the reconstruction of phase values from phase differences *J. Opt. Soc. Am.* **69** 393–9

[30] Schmidt J D 2010 *Numerical Simulation of Optical Wave Propagation with Examples in MATLAB* (Bellingham, Washington: SPIE Press)

[31] Rasouli S, Niry M D, Rajabi Y, Panahi A A and Niemela J J 2012 Measuring anisotropy in atmospheric turbulence by means of moiré deflectometry *Phys. Rev.* E submitted